Research Network FWF S105

Photoacoustic Imaging in
Medicine and Biology

http://www.csc.univie.ac.at/pai/

On the Use of Frequency-Domain Reconstruction Algorithms for Photoacoustic Imaging

Rainer Schulze, Gerhard Zangerl, Markus Holotta, Dirk Meyer, Florian Handle, Robert Nuster, Günther Paltauf and Otmar Scherzer

March 2011

PAI Report No. 35

Der Wissenschaftsfonds.

On the Use of Frequency-Domain Reconstruction Algorithms for Photoacoustic Imaging

Rainer Schulze[1,*], Gerhard Zangerl[2], Markus Holotta[3], Dirk Meyer[4], Florian Handle[6], Robert Nuster[5], Günther Paltauf[5], and Otmar Scherzer[1,2]

[1]Johann Radon Institute for Computational and Applied Mathematics, Austrian Academy of Sciences, Austria
[2]Computational Science Center, University of Vienna, Austria
[3]Medical University Innsbruck, Department Radiology, Austria
[4]Leopold-Franzens University Innsbruck, Institute for Molecular Biology, Austria
[5]Karl-Franzens University Graz, Institute for Physics, Austria
[6]Medical University Innsbruck, Internal Medicine I, Austria
[*]Corresponding author: Rainer.Schulze@uibk.ac.at

March 24, 2011

Abstract

We investigate the use of a frequency-domain reconstruction algorithm based on the Nonuniform Fast Fourier Transform (NUFFT) for Photoacoustic Imaging (PAI). Standard algorithms based on the FFT are computationally efficient but compromise the image quality by artifacts. In our previous work we have developed an algorithm for PAI based on the NUFFT which is computationally efficient and can reconstruct images with the quality known from temporal back-projection algorithms. In this paper we review imaging qualities, such as resolution, signal-to-noise ratio, and the effects of artifacts in real-world situations. Reconstruction examples show that artifacts are reduced significantly. In particular, image details with a larger distance from the detectors can be resolved more accurately than with standard FFT algorithms.

Keywords: Photoacoustic Imaging, detectors, reconstruction algorithms, imaging properties

Photoacoustic Imaging (PAI) is cross-sectional or 3D imaging based on the photoacoustic effect. PAI combines the advantages of optical imaging contrast with ultrasonic spatial resolution. In [1] the reader can find an overview of current state of the art imaging modalities.

The combination of accurate detectors and efficient reconstruction algorithms is crucial for a successfully operating PAI system. Frequency domain algorithms are computationally efficient because they usually rely on an implementation with the Fast Fourier Transform (FFT). The standard FFT algorithm has the major drawback that it requires a uniform sampling of data points, while the back-projection formula for the photoacoustic inverse problem, described below, requires a nonuniform sampling. Several proposals exist to overcome this problem. In this work we focus on a novel inversion scheme based on the Nonuniform FFT (NUFFT) as described in [2]. The NUFFT has been introduced in [3], and the combination with the inverse Radon transform for solving tomographic problems was described in [4].

This paper is organized as follows: In Sec. 1 we give an overview of our experimental setup from which the data was obtained. Then we review the mathematics of the NUFFT reconstruction algorithm in Sec. 2. The most relevant section is Sec. 3, where we investigate how imaging properties are affected by the use of the novel algorithm. There, we show its accuracy when applied to clinically and biologically relevant examples. Finally, in Sec. 4 we conclude our work by a final discussion of the investigated algorithms.

1 Experimental setup

In this section we give a short description of our experimental setup used to acquire the data for our studies. Our setup is equipped with an integrating line detector for acquiring the measurement data (see [5] for a description of the setup). Integrating line detectors increase the image quality with respect to the resolution and occurring reconstruction artifacts, especially if a free-beam interferometric setup is used [6, 7]. The integrating detector used in the presented studies is realized with a free-beam Mach-Zehnder interferometer (MZI). Optical beams as part of an interferometer have omni directional response [7], but need focusing in order to achieve high temporal and spatial resolution. Our focus was well below 60 μm along the focal length. Finally, the actual resolution limit is determined by the sampling density, the involved electronics and penetration depth. Typical values are 80-120 μm [8].

The setup is shown in Fig. 1. The emerging ultrasound waves propagate through a tank filled with water which acts coupling medium between sample and detector. The pressure wave leads to a change in the refractive index of the water and therefore causes a phase shift in the measurement beam of the MZI. The interferometer is actively stabilized by a piezo-controlled mirror, which counteracts slow oscillations as well as long-term drift. Since the optical components have to be stabilized, it is necessary to move the sample relative to the beam. As pump laser, we used an optical parametric oscillator (OPO) pumped by an Nd:YAG laser system (Surelite II-10, Continuum, Santa Clara, USA).

Data acquisition for a complete 3D dataset consists of two steps: First, the sample is moved to a fixed detector position and rotated about 360°. The photoacoustic transient is recorded for each laser pulse at equidistant angular positions. Having recorded the signals for all angles and detector positions, a 3D dataset can be generated as described below.

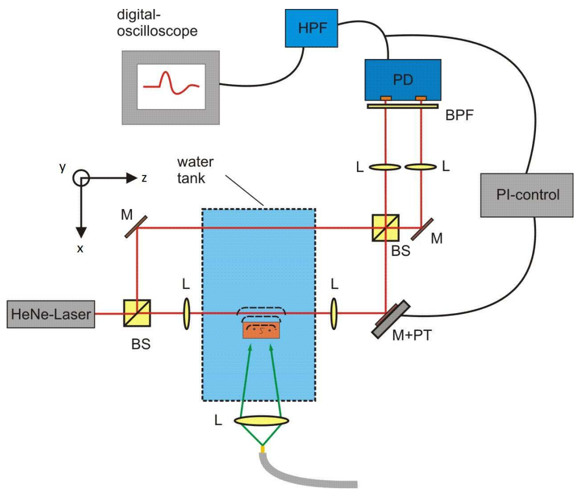

Figure 1: (Color online) Schematic of experimental setup. Ultrasound waves are detected with a free-beam MZI. BS: beam splitter, M: mirror, M+PT: piezo-stabilized mirror, L: lens, BPF: band-pass filter, PD: photo diodes, HPF: high-pass filter.

2 Mathematical review

In order to describe the data acquisition process outlined above we assume that a Cartesian coordinate system is placed beside an object that is rotated by an angle α. Furthermore, we assume that the linear integrating detector moves along the $y-$axis as described in figure 2. If p_α denotes the pressure that is emitted by the rotated object, described by $p_{0\alpha}$, the measurement data are given by

$$q(y_d, t) = \int_{\mathbb{R}} p_\alpha(0, y_d, z, t) dz, \tag{1}$$

From this data it is possible to obtain the projection

$$q_{0\alpha}(x, y) = \int_{\mathbb{R}} p_{0\alpha}(x, y, z) dz \tag{2}$$

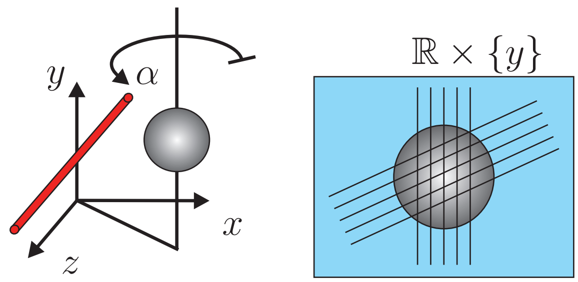

Figure 2: (Color online) Left: Pressure integrals over lines parallel to the $z-$axis running through $(0, y_d, 0)$ are collected from an object that has been rotated by an angle α. Right: Rotating the parallel family of lines instead of the object yields the Radon transform in each plane $\mathbb{R} \times \{y\}$.

of the rotated object over the family of lines running through (x, y) that are parallel to the $z-$axis. Since it would be equivalent to fix the object and rotate the family of lines instead the projections $(q_{0\alpha})$ provide the Radon transform in each plane $\mathbb{R} \times \{y\}$, see figure 2.

Inverting the 2D Radon transform in each pane gives the desired 3D reconstruction. In the following we will focus on the reconstruction of a single projection and thus will omit α in the following.

The first FFT-based inversion scheme for a similar photoacoustic inverse problem using point detectors was proposed in [9]. For our case the back-projection identity reads

$$Q_0(k_x, k_y) = \frac{2ck_y}{\operatorname{sign}(k_y)\sqrt{k_x^2 + k_y^2}} Q\left(k_x, c \cdot \operatorname{sign}(k_y)\sqrt{k_x^2 + k_y^2}\right), \tag{3}$$

where $Q(k_x, \omega)$ is the Fourier transform of the measured data $q(x_d, \cdot, t)$ and $Q_0(k_x, k_y)$ is the Fourier transform of the projections $q_0(x, y)$. In order to derive this, the dispersion relation $k_y = \sqrt{(\omega/c)^2 - k_x^2})$ was used.

It seems a straightforward step to apply the FFT to the data, scale it back in frequency space using (3), and apply the FFT again. However, for equally spaced samples of the frequency the use of this dispersion relation implies that the k_y are sampled non-equidistant. In other words, the back-projection in frequency domain via the dispersion relation requires nonuniform sampling of the frequency data points used in the inverse transform. In order to apply FFT algorithms, which assume sampling on an equidistant grid, the data points have to be resampled via interpolation before transforming back to position space. As discussed in all the works cited above, interpolation in Fourier space causes considerable artifacts.

One can avoid this problem by using the Discrete Fourier Transform (DFT)

$$T[\mathbf{g}](\omega_k) := \sum_{n=0}^{N-1} e^{-i\omega_k n2\pi/N} g_n \tag{4}$$

where $\mathbf{g} = (g_n)_{n=0}^{N-1} \in \mathbb{C}$. Note that by expressing the DFT as above, we do not necessarily impose $\omega_k = k\omega$ as is usually done. Therefore, this sum allows the nodes $(\omega_k)_{k=N/2}^{N/2-1}$ to be sampled on an arbitrary grid. Evaluating the sums in (4) requires $\mathcal{O}(N^2)$, which of course does not lead to a fast algorithm. When using the NUFFT algorithm as presented in [4] we have two choices:

- apply standard FFT to the data, then do the inverse transform on a nonuniform grid (via the NUFFT),
- apply NUFFT to the data at non-equidistant grid points in order to get non-equidistant results in frequency domain, then do the equidistant inverse Fourier transform.

The first case is called NED (non-equispaced data) and the second case is called NER (non-equispaced results). As discussed in the reference, the second option is easier to implement and provides a faster algorithm.

In the following we will summarize the results obtained in [2]. Let $\Psi : \mathbb{R} \to \mathbb{R}$ an appropriate function that satisfies:

1. Ψ is continuous inside $[-\alpha, \alpha]$,
2. Ψ is supported in $[-\alpha, \alpha]$
3. Ψ is positive in $[-\pi, \pi]$,

and let $\hat{\Psi} := \mathcal{F}\{\Psi\}$ its Fourier transform. Ψ is called window function. With this definition, we are ready to explain the NUFFT algorithm, which is based on the identity

$$\sum_{n=0}^{N-1} e^{-i\omega n2\pi/N} g_n = \sum_{j\in\mathbb{Z}} e^{-i\pi(\omega-j/c)} \hat{\Psi}(\omega - j/c)\hat{G}_j \,, \tag{5}$$

with

$$\hat{G}_j := \frac{c}{2\pi} \left(\sum_{n=0}^{N-1} \frac{g_n e^{-ijn2\pi/(Nc)}}{\Psi(n2\pi/N - \pi)} \right) , \qquad j \in \mathbb{Z} \,, \tag{6}$$

where $c > 1$ is an oversampling factor, $\alpha < \pi(2c-1)$ is the window size and $(g_n)_{n=0}^{N-1} \in \mathbb{C}^N$ is the vector containing the data. Equation (5) expresses the Fourier transform of the signal g_n evaluated at an arbitrary frequency ω.

The window function $\hat{\Psi}$ has to be chosen such that it is concentrated around zero (and decaying rapidly away from zero). Then in the summation on the right hand side of (5) only a few terms have to be taken into account. This is the main approximation in NUFFT-based algorithms. According to the above references, the Kaiser-Bessel window function is the best choice such that the approximation error is small. It is also important to note that we impose $cN \in \mathbb{N}$, which allows us to expand the summation in (6) to $[0, cN-1]$. Then, the equation represents an oversampled discrete Fourier transform. This allows us to apply the standard FFT in this step of the reconstruction algorithm simply by appending $(c-1)N$ zeros to the data vector g_n.

For further analysis we refer the interested reader to the publication by Haltmeier et al. [2].

3 Applications

The improvements achieved by NUFFT reconstruction are demonstrated below using several biological and clinical examples. All data were generated with the PAI system described above. We examined:

- sutures in order to test whether the use of the algorithm influences the image resolution limit
- mouse mammary-carcinoma
- zebrafish embryos 2 days-post-fertilization (dpf).

Only detector array geometries which fulfill the conditions of the theoretical derivations are stable. Unstable reconstructions suffer from artifacts in the projection images. Mainly, pressure values below zero are generated in the final image and appear either as shadow-like artifacts or an inhomogeneous background. For the application of FFT-based back projection algorithms as described above this has the implication that the detector array positions must lie on an infinite straight line, as Eq. 3 has been derived under this condition. Of course, infinite detector arrays do not exist in reality. Even if approximating by an array length much larger than the sample size produces severe artifacts. Therefore it was suggested to make two linear scans perpendicular to each other such that the detector array encloses the object with a triangle [6]. Even better is a box-scan, consisting of three linear scans (in the directions upward, forward and downward the sample) [10]. The two or three reconstructed images are then superimposed. We used the box scan detector configuration in all examples discussed below. See also Fig. 3.

All source code was written in MATLAB (MathWorks, Natick, Massachusets, USA) and the reconstructions were processed on a standard 64-bit personal computer. The window function Ψ and its Fourier transform were pre-computed and stored. Computation of a 300×300 px image using the FFT routine took 0.151 s. The NUFFT routine took 0.120 s without, and 0.252 s with pre-computations. Notice that without pre-computations, runtimes are comparable.

As described in the following paragraphs, we could show that the image quality obtained via the NUFFT algorithm is superior to the FFT-reconstructed images.

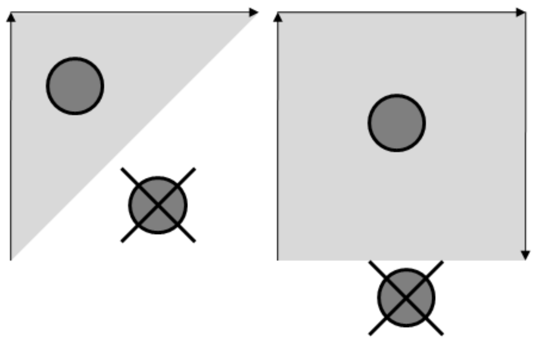

Figure 3: Sketch of our scanning geometries. Depicted are an L-Scan geometry (left) and a box-scan geometry (right). The shaded gray areas represent the set of coordinates where a stable reconstruction is possible.

3.1 Resolution and image quality

As an important remark we point out that the experimental resolution limit should not be affected by the use of different algorithms. We test the resolution limit in the two images to outrule the possibility that either Fourier domain algorithm causes smearing artifacts.

We measured clinical sutures with a diameter of 50 µm. This is below the resolution limit of our system and therefore we can obtain a resolution limit by fitting a Gaussian distribution to the gray value profile of the sutures. In order to resolve the Gaussian, the pixel (voxel) size has to be significantly smaller than the anticipated spatial resolution limit. In this case, the pixel size was 27 µm. Commonly, one uses full-width-half-maximum (FWHM) of the Gaussian to quantize the resolution performance of an imaging system. Therefore, the fitting function $\rho(x)$ reads

$$\rho(x) = A \exp\left(-\frac{4\log(2)(x-x_0)^2}{x_{\mathrm{FHWM}}^2}\right). \tag{7}$$

The signals of two sutures lying side by side are depicted in Fig. 4. A curve fit has been applied to the normalized FFT and NUFFT gray value profiles. The fit to the FFT data gives 125 µm and 138 µm for the left and right suture respectively, giving an average of 131.5 µm at FWHM. The fit to the NUFFT data gives 121 µm and 131 µm for the left and right suture respectively, giving an average of 126 µm at FWHM. As the suture does not imitate a perfect point-spread function, i. e. a Dirac δ-function, the actual resolution limit is below the above values. Note that subtraction of the suture diameter as was done for example in [11] does not give a correct resolution performance of an imaging system in general since the finite suture diameter and detector size lead to a deconvolution problem.

Differences in resolutions using different reconstruction algorithms typically range about 10 μm as can be seen in [6, page S90]. Using 95% confidence bounds gives a confidence interval of 114-150 μm for the FFT data and 108-144 μm for the NUFFT data. We conclude that the resolution limit is not affected significantly by the use of either algorithm as expected.

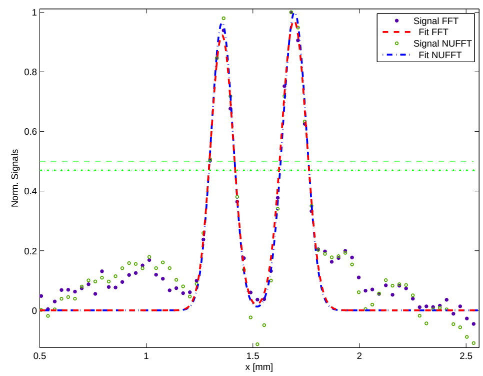

Figure 4: (Color online) Normalized gray value profiles and Gaussian fits of two sutures (diameter 50 μm). On average, the resolution limits are 81.5 μm (FFT algorithm) and 76 μm (NUFFT algorithm). For a confidence level of 95% the goodness of the fits is given by $R^2 = 0.871$ (FFT algorithm) and $R^2 = 0.887$ (NUFFT algorithm). We also show the FWHM values as horizontal lines (NUFFT... dashed line; FFT... dashed-dotted line).

Concerning image quality, we measured sutures of different diameters lying close to each other. We used sutures of diameters 20 μm, 50 μm and 70 μm. The images are displayed in Fig. 5. The measurement could not be used to determine the resolution limit due to the fact that the neglected nonuniform sampling in the FFT algorithm causes images to be biased towards the detector (which would be located in the upper edge of the images). As a consequence the 50 μm suture, which was tied to a ribbon, is not resolved completely by the FFT algorithm at all. The lower part of the ribbon is missing.

Another important aspect is that the shadow-like artifacts caused by the FFT algorithm are eliminated by the use of the NUFFT algorithm.

We also determined the signal-to-noise ratio (SNR) in both images. As reference, we chose the signal maximum of the 70 μm suture. We obtained an SNR of ∼43 for the FFT image and ∼42 for the NUFFT image. This clearly shows that the SNR itself is not improved by the use of the NUFFT algorithm. In image analysis the contrast-to-noise ratio (CNR) is important too. It is given by

$$\mathrm{CNR} = \frac{\langle S_s \rangle - \langle S_b \rangle}{\sigma} \tag{8}$$

where $\langle S_s \rangle$ is the mean value of the (suture) signal, $\langle S_b \rangle$ is the mean value of the background noise, and σ its standard deviation [11]. The resulting CNR's were $\sim$34 for the FFT algorithm and $\sim$38 for the NUFFT algorithm. The quantities are again comparable, but it seems that using the NUFFT algorithm improves the CNR slightly.

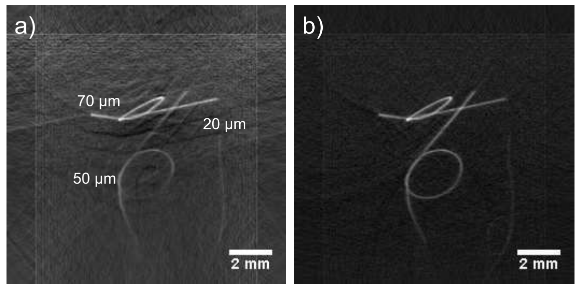

Figure 5: Sutures of diameters 20 μm, 50 μm and 70 μm reconstructed a) with the FFT algorithm and b) with the NUFFT algorithm. Observe that the suture bound to a ribbon (diameter 50 μm) is clearly visible in the NUFFT image, whereas its lower part is missing in the FFT image.

3.2 Test on biological samples

Let us begin by explaining the methods used to obtain our samples. Tumor bearing MMTV-neu mice were obtained from the Central Laboratory Animal Facility of the Innsbruck Medical University (Innsbruck, Austria). Female individuals serve as a model system for breast cancer and develop one or more tumors along the mammary ridges at an age of about 5 to 7 month. A detailed description of the mouse strain can be found in Guy et al and Parajuli et.al. [12, 13]. Mice were euthanized by CO2 and sacrificed by cervical dislocation. The tumors were excised and transferred into formaldehyde immediately for conservation. For measurements the tumors were embedded into agar and provided with a stick to enable mounting on the translational stage. All animals were treated in accordance with the Austrian animal welfare law and animal experiment act.

A main motivation for improving the reconstruction algorithm was to increase resolution of small structures such as zebrafish embryos. In first place the weak signals obtained from 2 day old zebrafish embryos could not be resolved in accurate detail (Fig. 7). The images in the first row represent the first sample, embedded in agar and measured with a box side length of 19 mm. The images in the second row represent the second sample, which was measured with a length of 13 mm because the agar cylinder could be reduced in diameter for this sample. We see the consequences of two important effects: The high frequencies caused by the small structures suffer from ultrasound attenuation in water. This is a well-known effect [14]. Therefore reducing the box side length and thus reducing the probe-detector distance considerably increased the image

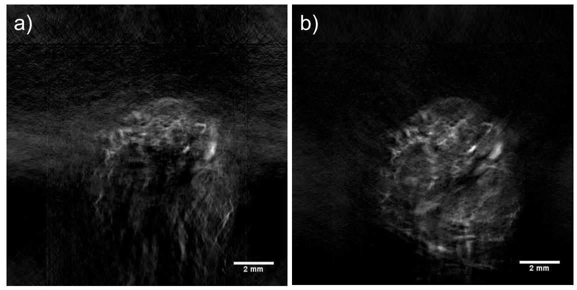

Figure 6: Box-scan projection images of an *ex vivo* mouse carcinoma. a) FFT reconstruction. b) NUFFT reconstruction. The background in the FFT image appears blurred, whereas in the NUFFT image it is more homogeneous.

quality. Again the homogeneity of the NUFFT images is better than that of the regular FFT images. The most important observation is that the embryos most far from the detector (lowest regions in the images) appear blurred and distorted in the FFT images. In the final configuration, i. e. 13 mm box length and use of the NUFFT algorithm, the reconstructed image corresponds very well with the microscopy image.

4 Conclusion and Outlook

In summary we have shown that the Nonuniform FFT reconstruction algorithm indeed provides superior image quality when compared to the standard FFT algorithm. This concerns artifacts as well as background gray values, which appear more homogeneous for the NUFFT images. We found that resolution and SNR (CNR) are not significantly improved by the use of the NUFFT over the standard FFT. The most capital improvement of the NUFFT reconstruction is its capability to reliably resolve image details that are farther away from the detector than about half the total image distance. In Tab. 8 we give the pros and cons for the two Fourier algorithms in summary.

Acknowledgment

This work has been supported by the Austrian Science Fund, projects No. S 10502-N20, S 10505-N20, S 10508-N20 and S 10509-N20. We thank Sonja Töchterle from the University of Innsbruck for her help with the zebrafish samples.

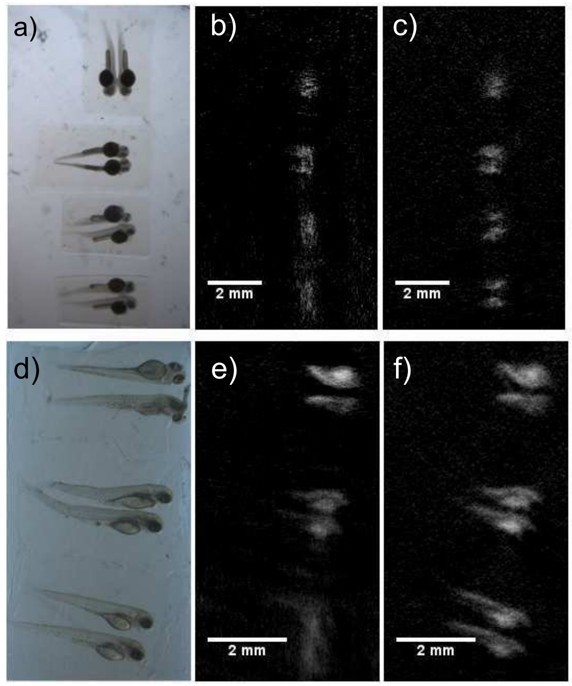

Figure 7: Box-scan of 2 day old zebrafish embryos. Two samples; sample 1 measured with box length 19 mm, sample 2 with 13 mm. a) microscope image of sample 1, b) reconstructed with FFT algorithm, c) reconstructed with NUFFT algorithm. d) microscope image of sample 2, e) reconstructed with FFT algorithm, f) reconstructed with NUFFT algorithm. Zebrafish embryos were grown as described in [15]. Scanning was performed with PFA-fixed embryos (a-c) or life embryos (d-f) embedded in 1,5% low melt agarose.

References

[1] L.V. Wang, "Prospects of photoacoustic tomography," Med. Phys. **35** (12) 5758-5767 (2008)

[2] M. Haltmeier, O. Scherzer, G. Zangerl, "A Reconstruction Algorithm for Photoacoustic Imaging Based on the Nonuniform FFT," IEEE Transactions on Medical Imaging **28**, no.11, 1727-1735 (2009)

[3] A. Dutt and V. Rokhlin, "Fast Fourier transforms for nonequispaced data," SIAM Journal on Scientific Computing, **14** (6) (1993)

Standard FFT algorithm	
Pro	Contra
no pre-computations	distortions and shadow-artifacts biased towards detector array
NUFFT algorithm	
Pro	Contra
reduction of artifacts homogeneous reconstruction area	pre-computations take most time

Figure 8: Pros and cons of the investigated frequency domain algorithms.

[4] K. Fourmont, “Non-equispaced fast Fourier transforms with applications to tomography,” Journal of Fourier Analysis and Applications, **9** (5), 431–450 (2003)

[5] P. Burgholzer, C. Hofer, G. Paltauf, M. Haltmeier and O. Scherzer, “Thermoacoustic Tomography with Integrating Area and Line Detectors,” IEEE Transactions on Ultrasonics, Ferroelectrics and Frequency Control **52**, no.9, 1577-1583 (2005)

[6] G. Paltauf, R. Nuster, M. Haltmeier and P. Burgholzer, “Experimental evaluation of reconstruction algorithms for limited view photoacoustic tomography with line detectors,” Inverse Problems **23** S81-S64 (2007)

[7] R. Nuster, S. Gratt, K. Passler and G. Paltauf, “Comparison of optical and piezoelectric integrating line detectors,” Proc. SPIE **7177**, (2009)

[8] G. Paltauf, R. Nuster and P. Burgholzer, “Characterization of integrating ultrasound detectors for photoacoustic tomography,” Journal of Applied Physics **105** (10), 102026 - 102026-9 (2009)

[9] Y. Xu, D. Feng, and L. V. Wang, “Exact frequency-domain reconstruction for thermoacoustic tomography. I: Planar geometry,” IEEE Trans. Med. Imag. **21** (7), 823–828 (2002)

[10] M. Holotta, H. Grossauer, C. Kremser, T. Pavle, J. Völkl, G. Degenhardt, R. Esterhammer, R. Nuster, G. Paltauf and W. Jaschke, “Photoacoustic tomography of *ex vivo* mouse hearts with myocardial infarction,” Journal

of Biomedical Optics **16**, 3 (2011)

[11] R. Ma, A. Taruttis, V. Ntziachristos and D. Razansky, "Multispectral optoacoustic tomography (MSOT) scanner for whole-body small animal imaging," Optics Express Vol. **17**, No. 24, 21414-21426 (2009)

[12] C. T. Guy, M. A. Webster, M. Schaller, T. J. Parsons, R. D. Cardiff, and W. J. Muller, "Expression of the Neu Protooncogene in the Mammary Epithelium of Transgenic Mice Induces Metastatic Disease," Proceedings of the National Academy of Sciences of the United States of America **89**, 10578 (1992)

[13] N. Parajuli and W. Doppler," Precision-cut slice cultures of tumors from MMTV-neu mice for the study of the ex vivo response to cytokines and cytotoxic drugs," In Vitro Cell Dev. Biol. Anim **45**, 442 (2009)

[14] P.J. La Rivière, J. Zang, and M.A. Anastasio, "Image reconstruction in optoacoustic tomography for dispersive acoustic media," Optics Letters **31** (6), 781-783 (2006)

[15] M. Westerfield, "The Zebrafish Book," University of Oregon Press, Eugene, USA (1995)